JOURNAL OF THERMOPHYSICS AND HEAT TRANSFER
Vol. 22, No. 2, April–June 2008

Transition Criteria for Entropy Reduction of Convective Heat Transfer from Micropatterned Surfaces

G. F. Naterer*
University of Ontario Institute of Technology, Oshawa, Ontario L1H 7K4, Canada

DOI: 10.2514/1.33292

This paper develops an entropy-transition number for characterizing irreversibilities of external flow past micropatterned surfaces with controlled surface roughness. It is shown that embedded surface microchannels can reduce flow irreversibilities below a classical boundary-layer limit, due to drag reduction of slip-flow conditions within the microchannels. A surface-irreversibility ratio establishes the proportion of entropy production of slip-flow relative to no-slip conditions. Then an entropy-transition number is defined to characterize flow regimes in which the ratio decreases below unity, thereby indicating conditions in which surface micropatterning has an overall beneficial impact on energy conversion efficiency. Results are presented for various micropatterned surfaces. It is shown that slip-flow conditions within the embedded surface microchannels can overcome the additional friction irreversibility of more surface area, reducing the total entropy production up to 20% below the boundary-layer flow without microchannels. At lower Reynolds numbers, it is shown that the irreversibility ratio decreases (for example, down to 0.79) at a Reynolds number of 1200. The newly defined surface-irreversibility and entropy-transition numbers are shown to provide useful new parameters to characterize the boundary-layer irreversibilities of convective heat transfer.

Nomenclature

d	=	depth of the microchannel, m
Kn	=	Knudsen number (mean free path divided by a characteristic length scale)
K_1	=	slip coefficient
k	=	thermal conductivity, W/mK
L	=	length of the plate, m
n	=	number of microchannels
q'	=	heat flow per unit length, W/m
Re	=	Reynolds number
T	=	temperature, K
u	=	freestream velocity, m/s
W	=	width of the plate, m
W_s	=	width of the microchannel, m
ζ	=	surface parameter, d/W
λ	=	surface parameter, $(W_s + 2d)/W$
μ	=	dynamic viscosity, kg/ms
ϕ	=	irreversibility distribution ratio

Subscripts

w	=	wall
∞	=	ambient (freestream) value

I. Introduction

MICROSYSTEMS have experienced rapid growth of practical applications in various aerospace and other fields such as micropropulsion, microelectronics cooling, microfluid machinery, and so forth. Moving microtabs and microelectromechanical systems (MEMS) along aerodynamic surfaces have the promising potential to reduce drag and improve aircraft maneuverability. In this paper, external flow past micropatterned surfaces is examined analytically and numerically to optimize the geometrical configurations of embedded surface microchannels, by minimizing the entropy production of combined thermal and friction irreversibilities therein.

Microfluidic systems usually entail laminar flow, due to relatively low Reynolds numbers associated with micron and submicron length scales. Transition between the continuum (no-slip), slip-flow, and free-molecule regimes depends on the local Knudsen number. The Knudsen number represents a ratio of the mean free path to a characteristic length scale of the problem [1]. McNenly et al. [2] investigated slip-flow models for nonequilibrium processes near a solid boundary. This paper examines laminar external flow with wall slip conditions over micropatterned surfaces that contain embedded open microchannels. The external flow configuration involves mixed Knudsen numbers, due to slip-flow conditions within the microchannels and no-slip conditions adjacent to the microchannels. In past studies, Xu and Ju [3] developed a slip-flow model to examine rarefied gas effects near the boundary of a microfluidic chamber. It was shown that slip-flow effects can significantly alter the predicted species transport between the wall and gas. A temperature jump condition at the wall affected the gas-phase reaction rates, because energy exchange between the gas and wall was reduced in slip-flow conditions.

The magnitude of fluid slip at a wall is characterized by the tangential momentum accommodation coefficient (TMAC). Arkilic et al. [4] reported experimental data with various TMAC values for gas flows in contact with a silicon wall. Isothermal slip flows through microchannels were examined and TMAC values were presented at various Knudsen numbers. For nitrogen, argon, and carbon dioxide, TMAC values range between 0.75 and 0.85. Other TMAC values in finite difference modeling of microchannel flows with a first-order slip-flow condition were presented by Chen et al. [5], including experimental results reported previously by Pong et al. [6] and Arkilic et al. [4].

Pressure-driven flow and electro-osmosis (electrically driven flow) are two common ways of pumping fluids through microchannels. Challenges of the former approach include designing and fabricating pumps with traditional microfabrication materials of silicon and glass, as well as plugging induced by particles in the fluid. On the other hand, electrical fields have other disadvantages, such as impurities absorbed on the wall, electrical heat generation in the fluid, and high voltages required for operation. The electric field produces a force on the fluid near the wall, while inducing adsorption and desorption of ions. Recent advances have shown that

Received 5 July 2007; revision received 3 November 2007; accepted for publication 10 November 2007.

*Professor, Canada Research Chair in Advanced Energy Systems, Faculty of Engineering and Applied Science, 2000 Simcoe Street North. Associate Fellow AIAA.

thermocapillary pumping is another viable method of flow control in microchannels [7,8].

In addition to fluid pumping, the process of fluid mixing affects microsystem performance. Liu et al. [9] developed a method of passively enhancing fluid mixing by a serpentine microchannel with a C-shaped repeating unit. In experiments with phenolphthalein and sodium hydroxide solutions at Reynolds numbers between 6 and 70, results indicated that faster mixing rates and more uniform mixing are achieved with certain 3-D channel geometries. Also, higher mixing rates were measured at larger Reynolds numbers. It was observed that the curved microchannel produces 16 times more reacted phenolphthalein than a straight channel. Another passive method for mixing streams of pressure-driven flows in microchannels was outlined by Stroock et al. [10]. In this method, bas-relief structures were fabricated by planar lithography on the floor of the microchannel. The microchannel length varied logarithmically with the Peclet number.

When improving the thermal performance of fluids engineering systems, it is well known that entropy and the second law can provide valuable tools for design optimization. Higher energy efficiency can be achieved systematically through entropy-generation minimization [11] in applications to heat exchangers, aircraft subsystems, compressors, condensers [12], and so forth. System-level entropy analysis entails global parameters such as the mass flow rate and net heat supply, whereas computational fluid dynamics enables local design modifications through finite element/volume analysis [13–15]. This paper extends past second-law advances to examine microfluidic entropy production, so that surface-embedded microchannels in flow control applications [16] can be systematically optimized with respect to overall energy efficiency.

Various techniques have been developed in the past for heat transfer enhancement while simultaneously reducing surface friction and entropy production. Some examples include annular fins [17], corrugated surfaces [18], and other passive techniques in heat exchangers [19]. Also, numerical methods such as gradient-based techniques or adaptive response surface method optimization [20] have been used for complex geometrical configurations. Recent advances in microfluidics [1] and Blasius similarity solution modeling [21] suggest that no-slip configurations within microdevices offer a promising alternative for drag reduction and heat transfer enhancement. This paper develops a method of entropy-based surface microprofiling to take advantage of local slip-flow conditions within embedded surface microchannels for drag reduction. Surface-irreversibility and entropy-transition numbers will be defined for the optimization of the microchannel configurations.

II. Formulation of Boundary-Layer Flow and Heat Transfer

Consider the problem of external flow and convective heat transfer from a heated flat surface with embedded surface microchannels (see Fig. 1). When viewed from above, the alternating no-slip and slip-flow velocity profiles grow in the x direction. At a given x location, the changes of velocity magnitude in the y direction would occur by cross-stream diffusion. Compared against diffusion normal to the plate and forced convection in the streamwise direction, the cross-stream diffusion will be assumed negligible. If the top of the channel was closed, then a quadratic velocity profile would be obtained from a Poiseuille no-slip-flow solution [19]. However, the current problem involves an open top boundary, across which diffusion from the base of the boundary layer interacts with the microchannel flow below it.

The continuum assumption is valid within the microchannel when $Kn \leq 0.001$ (where the Knudsen number Kn refers to the ratio of the mean free path to a characteristic length scale of the microchannel). Free-molecular flow arises if $Kn \geq 10$. For cases between these two limits, the slip-flow regime exists in the range of $0.001 \leq Kn \leq 10$ and the transition region occurs for $0.001 \leq Kn \leq 1$. Like other transition instabilities such as the onset of turbulence, the transition to free-molecular motion is sensitive to any geometrical or flow perturbations. For flow conditions with Knudsen numbers between 0.01 and 0.1 in the microchannel, the fluid motion is governed by the continuum Navier–Stokes equations, subject to slip-flow boundary conditions at the wall. The slip coefficient K_1 can be expressed by the following normalized expression [1]:

$$K_1 = \left(\frac{2-\sigma}{\sigma}\right) Kn \cdot Re_x^{1/2} \tag{1}$$

where Re_x is the Reynolds number and σ is the tangential momentum accommodation coefficient [1].

As the Knudsen number increases with smaller microchannels, the probability of a fluid molecule striking another molecule (rather than the wall) falls, because the walls are closer together. A molecule may reflect repeatedly from a wall before colliding with another molecule traveling in the principal flow direction. Thus, the presence of the wall becomes more pronounced on the intermolecular interactions. During these interactions in slip-flow conditions, some molecules striking a wall will be reflected diffusely and others will be reflected specularly. The tangential momentum accommodation coefficient represents the fraction of molecules reflected diffusely from the wall. This coefficient depends on the fluid and solid surface parameters and other factors. It has been demonstrated experimentally to have values between 0.2 and 0.8 (Gad-el-Hak [1]). The remaining portion of molecules $(1-\sigma)$ is reflected specularly from the wall.

The velocity profile and its spatial gradient both change within an embedded microchannel in the streamwise direction. The effective slip coefficient will be determined from averaging in the z–y and x–y planes. The approximated slip coefficient in the slip-flow model yields the same total surface friction as that obtained through integration of the exact wall shear stress along the microchannel walls. Referring to Fig. 1, the flow consists of mixed Knudsen numbers within and above each open microchannel, and so the formulation consists of no-slip and slip-flow models. Within a microchannel, the characteristic length of the Knudsen number should contain both depth and width or a hydraulic-diameter-based length. Otherwise, internal flow within an open microchannel may entail no-slip conditions. For example, a wide microchannel with a submicron or nanoscale depth may produce a Knudsen number corresponding to the slip-flow regime if the channel depth is used, but no-slip conditions would be expected across most (or all) of the embedded microchannel.

Solutions to boundary-layer flow and convective heat transfer to/from a flat plate (Fig. 1) are well known and predicted by the Blasius similarity solution. In this solution, the stream function $f(\eta)$ satisfies the following reduced form of the streamwise momentum equation:

$$f'''(\eta) + \tfrac{1}{2} f(\eta) f''(\eta) = 0 \tag{2}$$

where

$$\frac{u}{u_\infty} = f'(\eta) \tag{3}$$

and

$$\eta = v\sqrt{\frac{u_\infty}{\nu x}} \tag{4}$$

In these equations, η and u_∞ refer to the similarity variable and freestream velocity, respectively. For the no-slip problem, the boundary conditions are $f'(0) = 0 = f(0)$ and $f'(\infty) = 1$. The same Blasius equation will be used for the slip-flow problem within the embedded microchannels, except that the following slip condition is used at the wall:

$$f'(0) = K_1 f''(0) \tag{5}$$

Using a standard Runge–Kutta procedure of numerical integration [19], the wall shear stress can be determined after differentiating the velocity profile as follows:

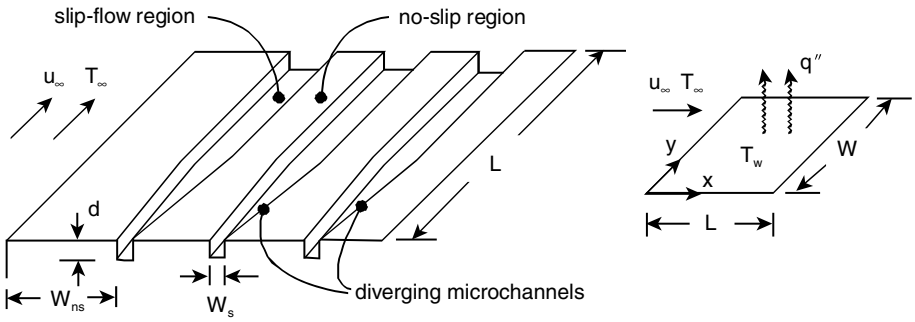

a)

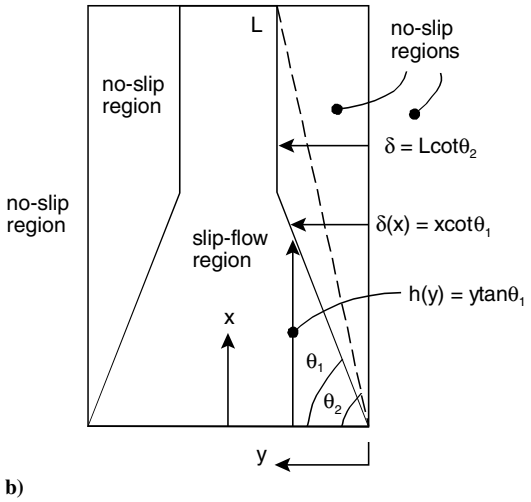

b)

Fig. 1 Embedded microchannels: a) side view and b) top view; θ_1 is the base angle and θ_2 is the exit angle.

$$\tau_w = \mu \left.\frac{\partial u}{\partial y}\right|_0 \tag{6}$$

$$\tau_w = \frac{\rho^{1/2}\mu^{1/2}u_\infty^{3/2}}{x^{1/2}} f''(0) \tag{7}$$

which can be rearranged as follows:

$$\frac{\tau_w}{\rho u_\infty^2} = \frac{f''(0)}{\sqrt{Re_x}} \tag{8}$$

The following analogous result is obtained for the Nusselt number:

$$Nu_x = \frac{hx}{k} \tag{9}$$

$$Nu_x = Re_x^{1/2} \cdot \theta'(0) \tag{10}$$

In the following sections, it will be determined whether the lower wall friction due to slip-flow conditions within an embedded surface microchannel is sufficiently offset by the added surface area of friction. Surface-irreversibility and entropy-transition parameters will be defined to characterize the net entropy production, including both thermal and friction irreversibilities.

III. Entropy Production and the Surface-Irreversibility Ratio

The total entropy production across a plate includes the irreversibilities of heat transfer over a finite temperature difference and fluid friction. For external flow, the total entropy production over a plate of length L and width W is given by [11,19]

$$\dot{S}_{\text{gen}} = \left(\frac{q''}{T_\infty}\right)^2 \int_0^W \int_0^L \frac{\mathrm{d}x\,\mathrm{d}y}{h} + \frac{u_\infty}{T_\infty} \int_0^W \int_0^L \tau_w \,\mathrm{d}x\,\mathrm{d}y \tag{11}$$

The previous correlations for convective heat transfer and wall shear stress are substituted into this equation. Consider parallel microchannels and define $\varsigma = d/W$ and $\lambda = (W_s + 2d)/W$. After performing the integrations in Eq. (11) for interspersed parallel sections of slip flow (within microchannels) and no slip (without microchannels), it can be shown that

$$\begin{aligned}\frac{\dot{S}_{\text{gen}}}{W} = {} & \left(\frac{q'^2}{kT_\infty^2}\right)[0.461K_1^{1.11}n\lambda + 2.008(1 + 2n\varsigma)]Re_L^{-1/2} \\ & + \left(\frac{u_\infty^2\mu}{T_\infty}\right)\left[\left(\frac{2.78}{4.185 + 0.96K_1^{1.11}}\right)n\lambda \right. \\ & \left. + 0.664(1 + 2n\varsigma - n\lambda)\right]Re_L^{-1/2}\end{aligned} \tag{12}$$

When performing the integration of entropy production over the entire plate, the regions are subdivided into slip-flow regions (n microchannels; integrated over $0 \le y \le W_s + 2d$) and the remaining no-slip regions (integrated over $0 \le y \le W - nW_s$). A slip-flow region can be further subdivided into a parallel microchannel section and a diverging section (integrated over $0 \le y \le \delta$; see Fig. 1). Similarly, the no-slip region can be subdivided into two distinct parts. When both parts are combined, the subdivided regions entail a slip-flow integral (n microchannels integrated over $0 \le y \le W_s + 2d$), no-slip integral (integrated over $0 \le y \le W - nW_s$), plus an integral involving slip minus no-slip integrands ($2n$ section integrated over $0 \le y \le \delta$). For linearly diverging microchannels, the result becomes

$$\frac{\dot{S}_{\text{gen}}}{W} = \left(\frac{q'^2}{kT_\infty^2}\right)\Bigg[(0.461K_1^{1.11}n\lambda + 2.008(1+2n\varsigma))Re_L^{-1/2} + \frac{0.921}{Re_W}nK_1^{1.11}\left(\cot\theta_2 - \frac{2}{5}\cot^{5/2}\theta_2\tan^{3/2}\theta_1\right)Re_L^{1/2}\Bigg] + \left(\frac{u_\infty^2\mu}{T_\infty}\right)\Bigg[\left(\frac{5.56}{4.185+0.96K_1^{1.11}} - 1.328\right)\frac{n}{Re_W} \times \left(\cot\theta_2 - \frac{2}{3}\cot^{3/2}\theta_2\tan^{1/2}\theta_1\right)\Bigg]Re_L^{3/2} + \left(\frac{u_\infty^2\mu}{T_\infty}\right)\Bigg[\frac{2.78n\lambda}{4.185+0.96K_1^{1.11}} + 0.664(1+2n\varsigma - n\lambda)\Bigg]Re_L^{1/2} \tag{13}$$

The second and third terms on the right side contain trigonometric factors and they are subtracted for the case of converging microchannels (see Fig. 1).

After the entropy production is computed, a surface-irreversibility ratio χ is defined as the ratio of entropy production for slip-flow (subscript s) to no-slip (subscript ns) conditions; that is,

$$\chi = \frac{\dot{S}_{\text{gen},s}}{\dot{S}_{\text{gen,ns}}} \tag{14}$$

It is desirable to generate a microprofiled surface that exhibits a surface-irreversibility ratio of less than unity. Otherwise, no benefit is realized when the entropy produced from slip-flow conditions (with additional surface area) exceeds the entropy production under regular no-slip conditions. The embedded surface microchannels add to a higher surface area, and so this additional resulting friction must be offset by drag reduction of local slip-flow conditions within the microchannels to achieve the smallest-possible surface-irreversibility ratios.

Using the previous result for entropy production over the plate with embedded diverging microchannels, the surface-irreversibility ratio becomes

$$\chi = \frac{(0.461K_1^{1.11}n\lambda + 2.008(1+2n\varsigma))q'^2/(k\mu u_\infty^2T_\infty) + (2.78n\lambda/(4.185+0.96K_1^{1.11}) + 0.664(1+2n\varsigma - n\lambda))Re_L}{(1+2n\varsigma)(2.008q'^2/(k\mu u_\infty^2T_\infty) + 0.664\,Re_L)} + \frac{0.921nK_1^{1.11}(\cot\theta_2 - 0.4\cot^{5/2}\theta_2\tan^{3/2}\theta_1)Re_Lq'^2/(k\mu u_\infty^2T_\infty)}{Re_W(1+2n\varsigma)(2.008q'^2/(k\mu u_\infty^2T_\infty) + 0.664\,Re_L)} + \frac{2(2.78/(4.185+0.96K_1^{1.11}) - 0.664)n(\cot\theta_2 - 0.667\cot^{3/2}\theta_2\tan^{1/2}\theta_1)Re_L^2}{Re_W(1+2n\varsigma)(2.008q'^2/(k\mu u_\infty^2T_\infty) + 0.664\,Re_L)} \tag{15}$$

The first term on the right side arises from the parallel section of embedded microchannels, and the latter two terms arise from the regions diverging outward from the parallel section (thereby exhibiting an angular dependence).

Minimizing the surface-irreversibility ratio leads to a surface micropattern that yields the lowest entropy production, relative to entropy produced under no-slip conditions. From Eq. (1), the slip coefficient depends on the momentum accommodation coefficient, Knudsen number, and Reynolds number. Minimizing the surface-irreversibility ratio with respect to the slip coefficient,

$$K_{1,\text{opt}} = \left(\frac{2.507}{q'}\sqrt{k\mu u_\infty^2T_\infty Re_L\left(\frac{1+2(\cot\theta_2 - 0.667\cot^{3/2}\theta_2\tan^{1/2}\theta_1)Re_L/(\lambda\,Re_W)}{1+1.997(\cot\theta_2 - 0.4\cot^{5/2}\theta_2\tan^{3/2}\theta_1)Re_L/(\lambda\,Re_W)}\right)} - 4.359\right)^{0.901} \tag{16}$$

The optimal slip coefficient K_1 becomes zero under the following condition:

$$Re_L = \frac{-a_2 + \sqrt{a_2^2 - 4a_1\cdot a_3}}{2a_1} \tag{17}$$

where

$$a_1 = \frac{13.118}{\lambda\,Re_W}\left(\frac{u_\infty^2\mu}{T_\infty}\right)\left(\cot\theta_2 - \frac{2}{3}\cot^{3/2}\theta_2\tan^{1/2}\theta_1\right) \tag{18}$$

$$a_2 = 6.559\left(\frac{u_\infty^2\mu}{T_\infty}\right) - \frac{0.922}{\lambda\,Re_W}\left(\frac{q'^2}{kT_{\infty^2}}\right)\left(\cot\theta_2 - \frac{2}{5}\cot^{5/2}\theta_2\tan^{3/2}\theta_1\right) \tag{19}$$

$$a_3 = -0.461\left(\frac{q'^2}{kT_{\infty^2}}\right) \tag{20}$$

Both slip-flow and no-slip conditions yield the same entropy production rate in this case. Alternatively, in terms of the applied surface heat flux,

$$q' = 3.772\,Re_Lu_\infty^2\mu kT_\infty \times \left(\frac{1+2(\cot\theta_2 - 0.667\cot^{3/2}\theta_2\tan^{1/2}\theta_1)Re_L/(\lambda\,Re_W)}{1+2(\cot\theta_2 - 0.4\cot^{5/2}\theta_2\tan^{3/2}\theta_1)Re_L/(\lambda\,Re_W)}\right) \tag{21}$$

At this particular heat flux, the reduced entropy production of slip-flow conditions is offset by added thermal irreversibility over a larger surface area with embedded microchannels.

Under certain flow conditions and geometrical parameters, it will be shown that the surface-irreversibility ratio decreases monotonically. This declining trend provides a useful sensitivity mechanism to determine how each parameter contributes to the desirable objective of minimizing the surface-irreversibility ratio. By differentiating the surface-irreversibility ratio with respect to a particular problem parameter, its sensitivity to changes of that parameter can be examined through magnitudes of the resulting slope of the differentiated variable. For instance, a large negative slope of the differentiated surface-irreversibility ratio with respect to the microchannel aspect ratio suggests an effective mechanism to reduce the entropy production by changing the aspect ratio. In the following section, the sensitivity coefficient will be called the entropy-transition number B (with a subscript to denote the sensitivity parameter). It will be determined based on a critical condition with a zero slope, which effectively separates the regions of increasing (undesirable) and decreasing (desirable) irreversibility ratios.

IV. Transition Criteria for Entropy Reduction

The entropy-transition number B represents a sensitivity of the surface-irreversibility ratio with respect to a particular problem parameter. For example, the entropy-transition number B_n is obtained by differentiating χ with respect to n and reorganizing the parameters to yield a zero derivative. From results in the previous section for parallel microchannels, the entropy-transition number with respect to the number of microchannels becomes

$$B_n = \frac{2\varsigma(2.008q'^2/(k\mu u_\infty^2 T_\infty) + 0.664\,Re_L)}{(0.461K_1^{1.11}n\lambda + 4.016\varsigma)q'^2/(k\mu u_\infty^2 T_\infty) + (2.78\lambda/(4.185 + 0.96K_1^{1.11}) + 0.664(2\varsigma - \lambda))Re_L} \tag{22}$$

In terms of its sensitivity to the microchannel aspect ratio, the sensitivity coefficient is

$$B_\varsigma = \frac{(0.461K_1^{1.11}n\lambda + 2.008)q'^2/(k\mu u_\infty^2 T_\infty) + (2.78n\lambda/(4.185 + 0.96K_1^{1.11}) + 0.664(1 - n\lambda))Re_L}{(2.008q'^2/(k\mu u_\infty^2 T_\infty) + 0.664\,Re_L)} \tag{23}$$

Values of unity signify a zero slope of the surface-irreversibility ratio. Values below unity yield a monotonically decreasing irreversibility ratio, which is desirable because it implies better effectiveness of the embedded surface microchannels in reducing entropy production over the plate. Values above unity give a monotonically increasing irreversibility ratio (undesirable).

For diverging microchannels, the entropy-transition number can be expressed as

$$B_n = \frac{2\varsigma}{\beta_{n,p} + \beta_{n,\mathrm{dh}} + \beta_{n,\mathrm{df}}} \tag{24}$$

where contributions from the parallel section of microchannels $\beta_{n,p}$, diverging section–thermal irreversibilities $\beta_{n,\mathrm{dh}}$, and diverging section–friction irreversibilities $\beta_{n,\mathrm{df}}$ are given by

$$\beta_{n,p} = \frac{(0.461K_1^{1.11}n\lambda + 4.016\varsigma)q'^2/(k\mu u_\infty^2 T_\infty) + (2.78\lambda/(4.185 + 0.96K_1^{1.11}) + 0.664(2\varsigma - \lambda))Re_L}{2.008q'^2/(k\mu u_\infty^2 T_\infty) + 0.664\,Re_L} \tag{25}$$

$$\beta_{n,\mathrm{dh}} = \frac{0.921K_1^{1.11}(\cot\theta_2 - 0.4\cot^{5/2}\theta_2\tan^{3/2}\theta_1)Re_L q'^2/(k\mu u_\infty^2 T_\infty)}{Re_W(2.008q'^2/(k\mu u_\infty^2 T_\infty) + 0.664\,Re_L)} \tag{26}$$

$$\beta_{n,\mathrm{df}} = \frac{2(2.78/(4.185 + 0.96K_1^{1.11}) - 0.664)(\cot\theta_2 - 0.667\cot^{3/2}\theta_2\tan^{1/2}\theta_1)Re_L^2}{Re_W(2.008q'^2/(k\mu u_\infty^2 T_\infty) + 0.664\,Re_L)} \tag{27}$$

In terms of the sensitivity to the microchannel aspect ratio,

$$\begin{aligned} B_\varsigma = {} & \frac{(0.461K_1^{1.11}n\lambda + 2.008)q'^2/(k\mu u_\infty^2 T_\infty) + (2.78n\lambda/(4.185 + 0.96K_1^{1.11}) + 0.664(1 - n\lambda))Re_L}{(2.008q'^2/(k\mu u_\infty^2 T_\infty) + 0.664\,Re_L)} \\ & + \frac{0.921nK_1^{1.11}(\cot\theta_2 - 0.4\cot^{5/2}\theta_2\tan^{3/2}\theta_1)Re_L q'^2/(k\mu u_\infty^2 T_\infty)}{Re_W(2.008q'^2/(k\mu u_\infty^2 T_\infty) + 0.664\,Re_L)} \\ & + \frac{2(2.78/(4.185 + 0.96K_1^{1.11}) - 0.664)n(\cot\theta_2 - 0.667\cot^{3/2}\theta_2\tan^{1/2}\theta_1)Re_L^2}{Re_W(2.008q'^2/(k\mu u_\infty^2 T_\infty) + 0.664\,Re_L)} \end{aligned} \tag{28}$$

Values of B_ζ above one give an increasing irreversibility ratio (undesirable) and values below one lead to a monotonically decreasing irreversibility ratio (desirable).

For the case of embedded converging microchannels (see Fig. 1), it can be shown that the following similar result is obtained for the entropy-transition number B_n:

$$B_n = \frac{2\varsigma}{\beta_{n,p} - \beta_{n,\mathrm{ch}} - \beta_{n,\mathrm{cf}}} \tag{29}$$

In this case, contributions from the parallel section $\beta_{n,p}$, converging section–thermal irreversibilities $\beta_{n,\mathrm{ch}}$, and converging section–friction irreversibilities $b_{n,\mathrm{cf}}$ are given by the following expressions:

$$\beta_{n,p} = \frac{(0.461K_1^{1.11}n\lambda + 4.016\varsigma)q'^2/(k\mu u_\infty^2 T_\infty) + (2.78\lambda/(4.185 + 0.96K_1^{1.11}) + 0.664(2\varsigma - \lambda))Re_L}{2.008q'^2/(k\mu u_\infty^2 T_\infty) + 0.664\,Re_L} \tag{30}$$

$$\beta_{n,\mathrm{ch}} = \frac{0.921K_1^{1.11}(\cot\theta_2 - 0.4\cot^{5/2}\theta_2\tan^{3/2}\theta_1)Re_L q'^2/(k\mu u_\infty^2 T_\infty)}{Re_W(2.008q'^2/(k\mu u_\infty^2 T_\infty) + 0.664\,Re_L)} \tag{31}$$

$$\beta_{n,\mathrm{cf}} = \frac{2(2.78/(4.185 + 0.96K_1^{1.11}) - 0.664)(\cot\theta_2 - 0.667\cot^{3/2}\theta_2\tan^{1/2}\theta_1)Re_L^2}{Re_W(2.008q'^2/(k\mu u_\infty^2 T_\infty) + 0.664\,Re_L)} \tag{32}$$

It can be verified that the proper limiting cases of no-slip conditions are obtained when the slip coefficient approaches zero.

Finally, the entropy-transition number with respect to the microchannel depth parameter B_ζ is obtained by differentiating the irreversibility ratio with respect to ζ and reorganizing the parameters to yield a zero derivative. For linearly converging embedded microchannels,

$$B_\zeta = \frac{(0.461K_1^{1.11}n\lambda + 2.008)q'^2/(k\mu u_\infty^2 T_\infty) + (2.78n\lambda/(4.185 + 0.96K_1^{1.11}) + 0.664(1-n\lambda))Re_L}{(2.008q'^2/(k\mu u_\infty^2 T_\infty) + 0.664\,Re_L)}$$
$$- \frac{0.921nK_1^{1.11}(\cot\theta_2 - 0.4\cot^{5/2}\theta_2\tan^{3/2}\theta_1)Re_L q'^2/(k\mu u_\infty^2 T_\infty)}{Re_W(2.008q'^2/(k\mu u_\infty^2 T_\infty) + 0.664\,Re_L)}$$
$$- \frac{2(2.78/(4.185 + 0.96K_1^{1.11}) - 0.664)n(\cot\theta_2 - 0.667\cot^{3/2}\theta_2\tan^{1/2}\theta_1)Re_L^2}{Re_W(2.008q'^2/(k\mu u_\infty^2 T_\infty) + 0.664\,Re_L)} \tag{33}$$

In addition to declining values of B_ζ, it is desired that the irreversibility ratio should fall below 1. Then the entropy production of the slip-flow surface will fall below the no-slip case. In the next section, sample numerical results will be presented for the entropy production, surface-irreversibility ratio, and entropy-transition number of various micropatterned surfaces.

V. Results and Discussion

In this section, numerical results will be presented for gas flows across various microprofiled surfaces (see the problem parameters in Table 1). In Fig. 2a, entropy production of airflow at 300 K past a micropatterned surface with 3300 parallel microchannels (90–deg expansion angles) is shown over a range of Reynolds numbers. The current numerical slip-flow formulation approaches the benchmark solution properly in the no-slip limit (when the slip coefficient becomes $K_1 = 0$), thereby providing useful validation of the numerical model. Also, close agreement is achieved between predicted results in the no-slip limit and experimental data (Czarske et al. [22]) with the measured wall shear stresses in the friction irreversibility portion of the total entropy production. The measured data represent changes of skin friction coefficients at varying Reynolds numbers in the no-slip-limit case. The results show that the entropy production at higher slip coefficients falls below the benchmark no-slip limit, thereby confirming the valuable utility of the drag reduction of embedded surface microchannels.

In Fig. 2b, entropy production with external flow of steam at 700 K and a wall heat flux of 100 W/m is presented. Again, the predicted entropy production in the no-slip limit (setting $K_1 = 0$ and $n = 0$ in the slip-flow formulation) correctly approaches the expected benchmark solution of a no-slip boundary layer without microchannels (documented in [11,19]). It can be observed that 2800 or 3000 embedded parallel microchannels lead to less entropy production than the minimum entropy production for the no-slip case. Thus, slip-flow conditions within embedded surface microchannels can successfully overcome the friction irreversibility of added surface area, thereby reducing the total entropy production below the classical external flow without microchannels. Figure 2b indicates that the entropy generation decreases with fewer embedded microchannels and shallower microchannel depths. In Figs. 2a and 2b, the cases with microchannels have a larger entropy production than no-slip-channel flow at lower Reynolds numbers (below 1000). The additional surface area of embedded microchannels leads to higher friction and entropy production at low Reynolds numbers, but slip-flow drag reduction within microchannels compensates and exceeds this effect of additional area when the Reynolds number becomes higher.

The predicted ratio of actual entropy production to the minimum entropy production (denoted by the entropy-generation number N_s) is shown in Fig. 3. Airflow at 300 K with base and exit expansion angles of 0.1 and 0.9 rad, respectively, are shown for diverging surface microchannels. Close agreement is achieved between the benchmark results of no-slip-plate flow without microchannels and predicted results from the slip-flow model in the no-slip limiting case ($K_1 = 0$). Moving leftward in Fig. 3 from the optimal ratio of L/L_{opt}, the thermal irreversibility increases (when a smaller surface area leads to a higher temperature difference between the wall and surrounding fluid) to transfer the fixed rate of heat flow q'. On the other hand, the friction irreversibility increases with a larger area of surface friction (when moving rightward from the optimal length ratio). Similar growth rates of each irreversibility are predicted for the range of heat fluxes and slip coefficients in Fig. 3. Smaller slopes near $L/L_{\text{opt}} > 1$ are observed for the cases with microchannels, because the slip-flow conditions reduce the growth rate of the rising friction irreversibility. At high ratios of L/L_{opt}, a lower entropy-generation number is predicted at $q' = 200$ W/m, because the thermal irreversibility decreases for lower wall heat fluxes. At small values of L/L_{opt} in Fig. 3, a larger value of the entropy-generation number is observed for cases with microchannels. This trend occurs because microchannels increase the surface area and friction, thereby leading to a larger entropy production at short plate lengths, unlike longer plate lengths (or higher Reynolds numbers for the same plate length) that allow slip-flow drag reduction to eventually offset the effects of higher friction from the additional area.

In Fig. 4, the optimal Reynolds number increases at higher values of the microchannel aspect ratio and slip coefficients. Airflow at 280 K is examined with a surface heat transfer rate of 5 W/m and parallel microchannels. Because the freestream velocity is specified (16 m/s), the different Reynolds numbers represent a varying plate length L. At higher aspect ratios, the microchannel depth and slip-flow area increases, and so the rising friction irreversibility at higher Reynolds numbers offsets the falling thermal irreversibility at longer plate lengths (due to the added slip-flow area). Also, drag reduction of higher slip coefficients leads to a larger optimal Reynolds number with a longer plate length.

The optimal plate length minimizes the exergy destruction of friction and thermal irreversibilities, thereby minimizing the net power required to deliver certain rates of heat exchange and mass flow across the surface. For Reynolds numbers below $Re_{L,\text{opt}}$, the friction irreversibility is reduced with a smaller surface area and net

Table 1 Summary of problem parameters for numerical studies

Figure	Parameters
2a	Air: $q' = 40$ W/m, $n = 3400$, $d/W = 0.00001$, $T = 300$ K, $U = 120$ m/s, and $W_s = 4$ μm
2b	Steam: $q' = 100$ W/m, K1 = 2, $(W_s + 2d)/W = 0.001$, $T = 700$ K, $U = 120$ m/s, and $W_s = 1$ μm
3	Air: $n = 10$, $d/W = 0.000001$, $\theta_1 = 0.1$ rad (5.7°), $\theta_2 = 0.9$ rad (51.6°), $T = 300$ K, and $U = 10$ m/s
4	Air: $q' = 5$ W/m, $(W_s + 2d)/W = 0.00006$, $T = 280$ K, $k = 0.025$ W/mK, and $U = 16$ m/s
5	Air: $q' = 200$ W/m, $K_1 = 0.1$, $\theta_1 = 0.4$ rad (22.8°), $\theta_2 = 0.5$ rad (28.5°), $T = 300$ K, and $U = 60$ m/s
6a	Helium: $n = 1000$, $(W_s + 2d)/W = 0.00002$, $d/W = 0.000002$, $T = 600$ K, and $U = 20$ m/s
6b	Helium: $n = 2200$, $\theta_1 = 0.2$ rad (11.4 deg), $\theta_2 = 0.7$ rad (39.9 deg), $T = 600$ K, and $U = 30$ m/s
7	Helium: $n = 1200$, $(W_s + 2d)/W = 0.00002$, $d/W = 0.000002$, $T = 600$ K, and $U = 20$ m/s
8a	Helium: $q' = 150$ W/m, $(W_s + 2d)/W = 0.00002$, $d/W = 0.000002$, $T = 600$ K, and $U = 30$ m/s
8b	Helium: $q' = 200$ W/m, $n = 3000$, $d/W = 0.0000001$, $T = 600$ K, and $U = 40$ m/s

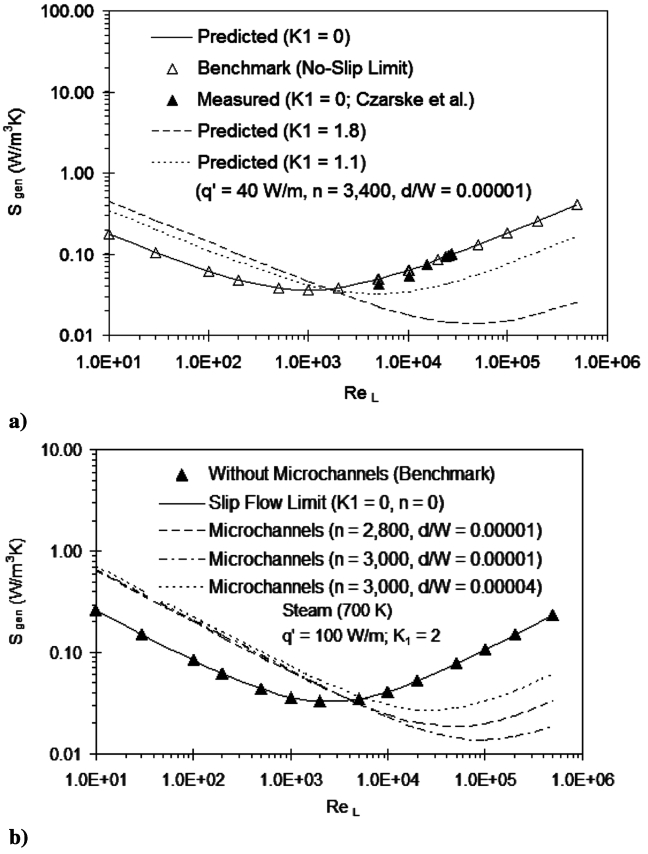

Fig. 2 Entropy generation at varying a) slip coefficients and b) aspect ratios.

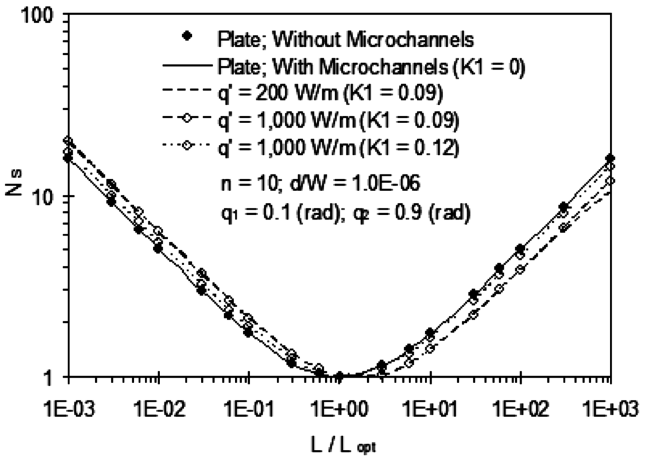

Fig. 3 Entropy-generation number for airflow at 300 K (diverging microchannels).

friction, but higher thermal irreversibilities arise due to a higher surface temperature and input power needed to transfer q' over a smaller area. On the other hand (values above $Re_{L,\mathrm{opt}}$), the thermal irreversibility decreases with a larger surface area available to transfer the fixed heat flow. But this reduction comes at the expense of higher friction irreversibility (when the larger surface area leads to added surface friction). Thus, the thermal irreversibility increases and the friction irreversibility diminishes when the surface length becomes larger, thereby yielding a crossover point at $Re_{L,\mathrm{opt}}$ at which entropy production is minimized. The thermal irreversibility is proportional to ΔT (temperature difference between the fluid and the wall) and q' (fixed), while being inversely proportional to T^2 (freestream temperature). The crossover point at the intersection of

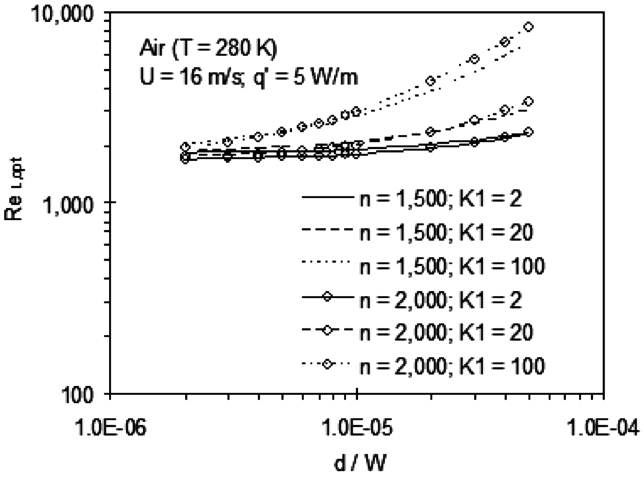

Fig. 4 Optimal Reynolds numbers at varying aspect ratios.

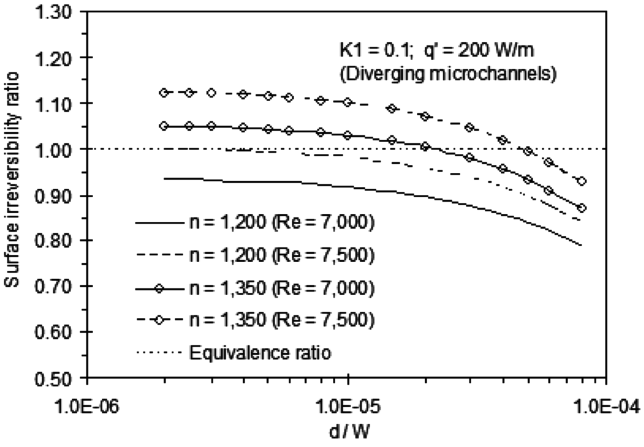

Fig. 5 Surface-irreversibility ratio χ for airflow at 300 K (diverging microchannels).

each irreversibility curve occurs at $Re_{L,\mathrm{opt}}$, which decreases when the freestream temperature rises.

In Fig. 5, diverging surface microchannels with base and exit expansion angles of 0.2 and 0.6 rad, respectively, are examined. The surface-irreversibility ratio decreases at higher microchannel aspect ratios, because more slip-flow area for deeper microchannels leads to lower entropy production, relative to the entropy production over the same surface area with no-slip friction. Also, Fig. 5 shows that the irreversibility ratio decreases with fewer microchannels and a lower Reynolds number at a specified microchannel depth. The thermal component of entropy production decreases at higher Reynolds numbers, because a lower temperature difference between the wall and fluid is needed to transfer a specified heat flow for larger plate areas. However, the friction irreversibility increases from added area and surface friction, and so the trends of the surface-irreversibility ratio depend on these combined factors.

As discussed earlier, it is desirable to establish the range of conditions yielding a decreasing rate of entropy production relative to the entropy produced without microchannels in no-slip conditions. This range depends on the geometrical configuration and flow parameters. A critical transition point occurs when the rate of change becomes zero, which is characterized by the sensitivity coefficient (called the entropy-transition number B). This critical condition will be illustrated as "monotonicity crossover" in the upcoming figures. Values below the monotonicity crossover give an decreasing rate of entropy production (desirable), and values above this crossover give a monotonically increasing rate (not desirable).

Figure 6 illustrates the change of B_n with varying slip coefficients, Reynolds numbers, and wall heat fluxes. The ratio of the parallel

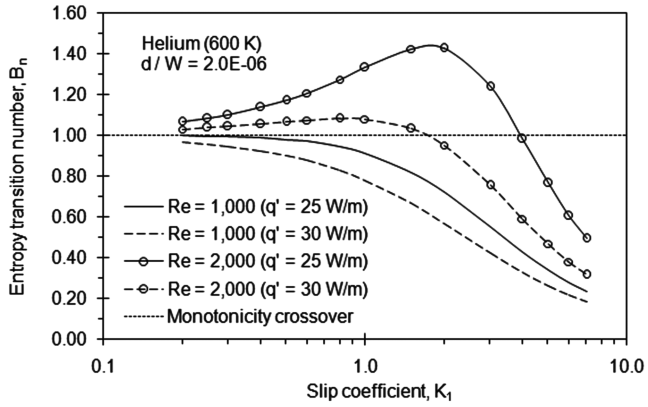

a)

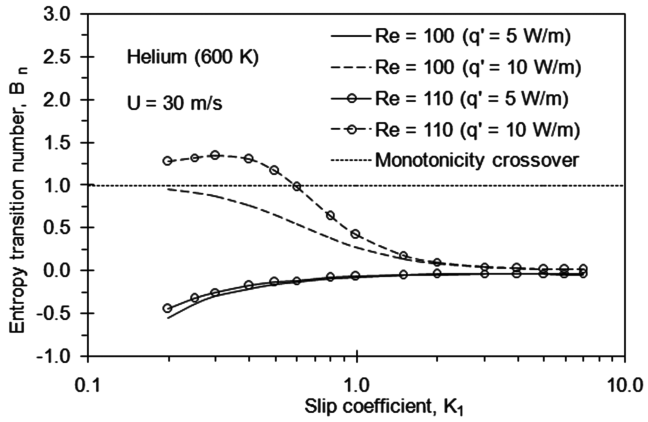

b)

Fig. 6 Entropy-transition number: a) parallel and b) diverging microchannels; $\theta_1 = 0.2$ rad.

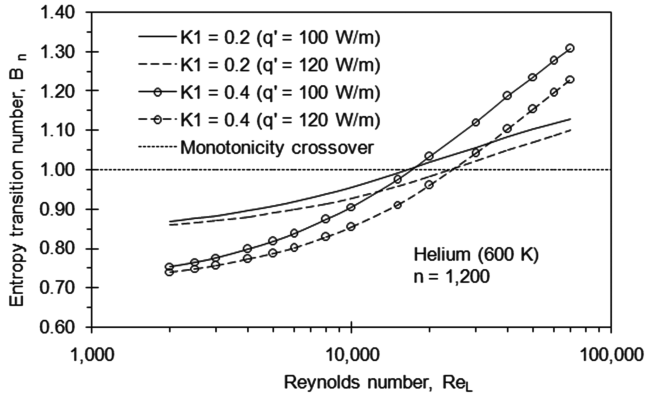

Fig. 7 Entropy-transition number at varying Reynolds numbers.

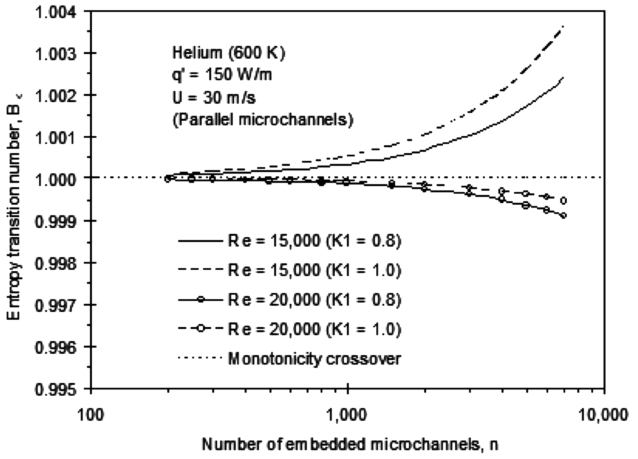

a)

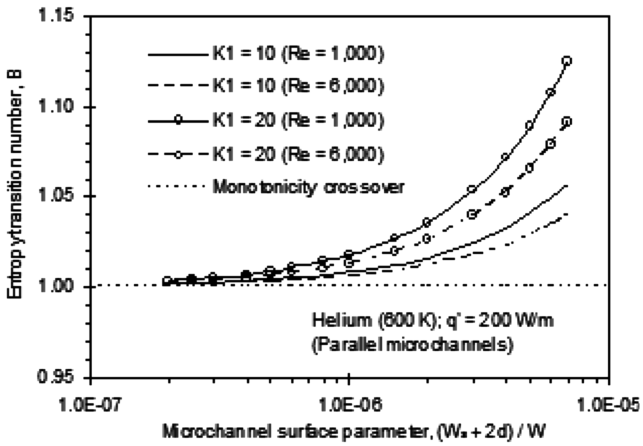

b)

Fig. 8 Sensitivity to a) number of microchannels and b) aspect ratio.

microchannel depth to plate width is 2.0×10^{-6}. Helium flow at 600 K is considered. In Fig. 6a, it can be observed that the entropy-transition number increases at low slip coefficients for the case of $Re = 2000$. The friction irreversibility increases with added surface area at higher Reynolds numbers, and the slip coefficient is too small for appreciable slip-flow effects of drag reduction. But B_n becomes negative at higher slip coefficients (when the slip-flow conditions have significant impact on reducing the friction irreversibilities). At the lower Reynolds number ($Re = 1000$), the smaller surface area leads to lower friction irreversibilities. As a result, the entropy-transition number is lower and it decreases at larger slip coefficients, due to the reduced drag of the higher slip at the wall. In Fig. 6b, the change of entropy-transition number is shown for cases of $q' = 5$ and 10 W/m. The entropy production increases up to about $K_1 = 0.6$ at the higher Reynolds number. The friction irreversibility increases for the larger surface area. Also, the thermal irreversibility increases in the case of the higher wall heat flux. But the higher irreversibility is offset by slip-flow conditions and drag reduction at higher slip coefficients (when the entropy-transition number becomes negative). For the case of $q' = 5$ W/m, the entropy production of embedded microchannels decreases faster, due to the lower thermal irreversibilities at the lower wall heat flux.

In Fig. 7, the set of curves corresponding to $K_1 = 0.2$ intersects the higher slip coefficient curves near the point of monotonicity crossover. For example, in Fig. 7, at q′ = 100 W/m, the $K_1 = 0.2$ curve intersects the $K_1 = 0.4$ curve at the monotonicity crossover. The thermal irreversibility decreases faster than the rising friction irreversibility at lower slip coefficients. Also, the entropy-transition number remains negative over a larger range of Reynolds numbers at higher heat fluxes. A higher magnitude of thermal irreversibility implies that its decreasing rate of change exceeds the rising rate of friction irreversibility at higher Reynolds numbers. The entropy production rises faster at higher slip coefficients, due to the lower friction irreversibility under slip-flow conditions. Also, it rises faster at higher wall heat fluxes, due to lower thermal irreversibilities. The thermal irreversibility is proportional to the wall heat flux and temperature difference (between the wall and surrounding fluid), while being inversely proportional to the freestream temperature. When the entropy-transition number remains below one, the beneficial effects of reduced entropy production can be realized. The ideal range of operating conditions should encompass both entropy-transition numbers and surface-irreversibility ratios below unity. The entropy produced along the embedded microchannel surface is then lower than the classical no-slip boundary-layer flow. Also, because the surface is exposed to a varying range of operating conditions, an entropy-transition number below unity is better suited to preserve the lower slip-flow entropy production, subject to the variability of flow conditions.

In Fig. 8a, the set of curves with $Re = 20,000$ occurs below the monotonicity crossover, due to the decreasing thermal irreversibility at higher Reynolds numbers. Above $B_\zeta = 1$, the entropy production rises slower at the lower slip coefficient, due to less drag reduction. Also, it can be observed that some cases between both Reynolds numbers and slip coefficients would lead to $B_\zeta = 1$, where the surface irreversibility remains constant at different surface parameters and numbers of embedded microchannels. The change of entropy production without microchannels matches the change with microchannels, and so the additional cost of manufacturing such surface microchannels could not be economically justified under those conditions.

In Fig. 8b, the change of entropy-transition number with varying surface parameters and Reynolds numbers is illustrated. The surface heat transfer rate is 200 W/m. In this case, B_ζ increases faster at lower Reynolds numbers, due to higher thermal irreversibility. When the surface area decreases, the temperature difference (between the wall and surrounding fluid) increases to transfer a fixed heat flow q'. Also, B_ζ increases at higher values of λ, because the added surface area contributes to higher friction irreversibility. These results indicate that the new parameters of surface-irreversibility ratio and entropy-transition number provide useful insight into the drag reduction and heat transfer enhancement for micropatterned surfaces.

Some practical criteria or guidelines for reducing entropy production with micropatterned surfaces would be shallow embedded microchannels with a small enough depth to yield local Knudsen numbers above 0.01 and slip coefficients above 1. Current results have generally shown entropy reduction under these conditions, although further studies are needed to extend the trends over a wider range of operating and flow conditions, including turbulence. The results have useful implications in various practical applications such as heat exchangers, cooling of microelectronic assemblies, and external flow configurations such as aerodynamic surfaces and heated airfoils on wind turbines and aircraft. An aerospace application was presented previously by Naterer et al. [16]. Controlled surface roughness with embedded microchannels can affect local flow separation from an aircraft surface, thereby allowing the local airstream to eject water from the surface before it refreezes downstream. Past studies have shown that surface microprofiling can be used for passive flow control involving the 1) position of flow detachment from the surface, 2) angle of flow detachment, and 3) frequency and magnitude of vortices shed from the detachment point and thereafter. Further extensions of the method to microactuated membranes within microchannels could be used to alter fine-scale structures within a boundary-layer flow. For example, actuated pulses within the microchannels could generate vortices that reduce or eliminate certain targeted flow structures. The embedded microchannels can be used like textured surfaces or riblets to reduce drag forces.

VI. Conclusions

In this paper, a newly defined parameter (called the entropy-transition number B) characterizes the sensitivity of a surface-irreversibility ratio to various parameters in convective heat transfer from micropatterned surfaces. Surface microprofiling reduces the total entropy production over the surface, due to drag reduction of slip-flow conditions within the microchannels. It is shown that slip-flow conditions within the embedded surface microchannels can overcome the additional friction irreversibility of more surface area, reducing the total entropy production up to 20% below the boundary-layer flow without microchannels. A higher surface-irreversibility ratio was found at larger values of $(W_s + 2d)/W$ (for example, up to 1.13 at a slip coefficient of $K_1 = 20$). The desirable range of operating conditions entails a decreasing rate of entropy production (when the entropy-transition number falls below unity). It is shown that B decreases at lower Reynolds numbers and higher slip coefficients. The entropy production decreases at lower Reynolds numbers for 1200 parallel microchannels, due to lower friction irreversibility over a smaller surface area. For a wall heat flux of 200 W/m, the surface-irreversibility ratio increases at higher values of the surface parameter λ. A critical range of wall heat fluxes and Reynolds numbers leads to an equivalent entropy production for both no-slip and slip-flow conditions. For both diverging and converging microchannels, the entropy-transition number decreases faster at lower wall heat fluxes. The entropy-transition number provides a useful new parameter to reduce entropy production of external flow past micropatterned surfaces.

Acknowledgments

Support of this research from Western Economic Diversification (WED), Westland Helicopters, Ltd., Canada Foundation for Innovation (CFI), and Natural Sciences and Engineering Research Council of Canada (NSERC) is gratefully acknowledged.

References

[1] Gad-el-Hak, M., "The Fluid Mechanics of Microdevices—The Freeman Scholar Lecture," *Journal of Fluids Engineering*, Vol. 121, 1999, pp. 5–33.

[2] McNenly, M. J., Gallis, M. A., and Boyd, I., "Slip Model Performance for Micro-Scale Gas Flows," AIAA 36th Thermophysics Conference, Orlando, FL, AIAA Paper 2003-4050, June, 2003.

[3] Xu, B., and Ju, Y., "Numerical Modeling of the Heterogeneous Combustion in a Micro Scale Chemical Reactor," AIAA 42nd Aerospace Sciences Meeting and Exhibit, Reno, NV, AIAA Paper 2004-0304, 2004.

[4] Arkilic, E. B., Breuer, K. B., and Schmidt, M. A., "Mass Flow and Tangential Momentum Accommodation in Silicon Micromachined Channels," *Journal of Fluid Mechanics*, Vol. 437, 2001, pp. 29–43. doi:10.1017/S0022112001004128

[5] Chen, C. S., Lee, S. M., and Sheu, J. D., "Numerical Analysis of Gas Flow in Microchannels," *Numerical Heat Transfer, Part A, Applications*, Vol. 33, 1998, pp. 749–762. doi:10.1080/10407789808913964

[6] Pong, K. C., Ho, C., Liu, J., and Tai, Y., "Non-Linear Pressure Distribution in Uniform Microchannels," *Application of Microfabrication to Fluid Mechanics (FED–1997)*, American Society of Mechanical Engineers, New York, 1994, pp. 51–56.

[7] Sammarco, T. S., and Burns, M. A., "Heat Transfer Analysis of Microfabricated Thermocapillary Pumping and Reaction Devices,'' *Journal of Micromechanics and Microengineering*, Vol. 10, 2000, pp. 42–55. doi:10.1088/0960-1317/10/1/307

[8] Sammarco, T. S., and Burns, M. A., "Thermocapillary Pumping of Discrete Drops in Microfabricated Analysis Devices," *AIChE Journal*, Vol. 45, 1999, pp. 350–366. doi:10.1002/aic.690450215

[9] Liu, R. H., Stremler, K. V., Sharp, M. G., Olsen, J. G., Santiago, R. J., Adrian, H., Aref, H., and Beebe, D. J., "Passive Mixing in a Three-Dimensional Serpentine Microchannel," *Journal of Microelectromechanical Systems*, Vol. 9, 2000, pp. 190–197. doi:10.1109/84.846699

[10] Stroock, A. D., Dertinger, S. K. W., Ajdari, A., Mezic, I., Stone, H. A., and Whitesides, G. M., "Chaotic Mixer for Microchannels," *Science*, Vol. 295, 2002, pp. 647–651. doi:10.1126/science.1066238

[11] Bejan, A., *Entropy Generation Minimization*, CRC Press, Boca Raton, FL, 1996.

[12] Stegou-Sagia, A., and Paignigiannis, N., "Exergy Losses in Refrigerating Systems. A Study for Performance Comparisons in Compressors and Condensers'', *International Journal of Energy Research*, Vol. 27, No. 12, 2003, pp. 1067–1078. doi:10.1002/er.936

[13] Naterer, G. F., "Constructing an Entropy-Stable Upwind Scheme for Compressible Fluid Flow Computations," *AIAA Journal*, Vol. 37, No. 3, 1999, pp. 303–312.

[14] Naterer, G. F., "Establishing Heat–Entropy Analogies for Interface Tracking in Phase Change Heat Transfer with Fluid Flow," *International Journal of Heat and Mass Transfer*, Vol. 44, No. 15, 2001, pp. 2903–2916.

[15] Naterer, G. F., and Camberos, J. A., "Entropy and the Second Law in Fluid Flow and Heat Transfer Simulation," *Journal of Thermophysics and Heat Transfer*, Vol. 17, No. 3, 2003, pp. 360–371.

[16] Naterer, G. F., Chomokovski, S. R., Friesen, C., and Shafai, C., "Micro-Machined Surface Channels Applied to Engine Intake Flow and Heat

Transfer," AIAA 36th Thermophysics Conference, Orlando, FL, AIAA Paper 2003-4054, 23–26 June 2003.

[17] Antar, M. A., "Steady and Transient Numerical Analysis of the Performance of Annular Fins,'' *International Journal of Energy Research*, Vol. 25, No. 13, 2001, pp. 1197–1206. doi:10.1002/er.748

[18] Zimparov, V., "Energy Conservation through Heat Transfer Enhancement Techniques,'' *International Journal of Energy Research*, Vol. 26, No. 7, 2002, pp. 675–696. doi:10.1002/er.810

[19] Naterer, G. F., *Heat Transfer in Single and Multiphase Systems*, CRC Press, Boca Raton, FL, 2002.

[20] Wang, D., Naterer, G. F., and Wang, G., "Thermofluid Optimization of a Heated Helicopter Engine Cooling Bay," *Canadian Aeronautics and Space Journal*, Vol. 49, No. 2, 2003, pp. 73–86.

[21] Martin, M. J., and Boyd, I. D., "Blasius Boundary Layer Solution with Slip Flow Conditions," *Rarefied Gas Dynamics: 22nd International Symposium*, Vol. 585, American Inst. of Physics, College Park, MD, July 2000.

[22] Czarske, J., Buttner, L., Razik, T., Muller, H., Dopheide, D., Becker, S., and Durst, F., "Spatial Resolved Velocity Measurements of Shear Flows with a Novel Differential Doppler Velocity Profile Sensor," 11th International Symposium on Applications of Laser Techniques to Fluid Mechanics, Lisbon, Portugal, 8–11 July 2002.